Journal of Biomechanics 58 (2017) 27–36

Contents lists available at ScienceDirect

Journal of Biomechanics

journal homepage: www.elsevier.com/locate/jbiomech
www.JBiomech.com

Local displacement and strain uncertainties in different bone types by digital volume correlation of synchrotron microtomograms

Marco Palanca [a], Andrew J. Bodey [b], Mario Giorgi [c], Marco Viceconti [d], Damien Lacroix [d], Luca Cristofolini [a], Enrico Dall'Ara [c,*]

[a] Department of Industrial Engineering, School of Engineering and Architecture, Alma Mater Studiorum - Università di Bologna, Via Terracini 24/28, Bologna 40131, Italy
[b] Diamond Light Source, Oxfordshire OX11 0QX, UK
[c] Department of Oncology and Metabolism and INSIGNEO Institute for In Silico Medicine, University of Sheffield, Sir Frederick Mappin Building, Pam Liversidge Building, Sheffield S1 3JD, UK
[d] Department of Mechanical Engineering and INSIGNEO Institute for In Silico Medicine, University of Sheffield, Sir Frederick Mappin Building, Pam Liversidge Building, Sheffield S1 3JD, UK

ARTICLE INFO

Article history:
Accepted 9 April 2017

Keywords:
Synchrotron
microCT
Digital volume correlation
Bone
Strain
Uncertainties

ABSTRACT

Understanding bone mechanics at different hierarchical levels is fundamental to improve preclinical and clinical assessments of bone strength. Digital Volume Correlation (DVC) is the only experimental measurement technique used for measuring local displacements and calculating local strains within bones. To date, its combination with laboratory source micro-computed tomography (LS-microCT) data typically leads to high uncertainties, which limit its application. Here, the benefits of synchrotron radiation micro-computed tomography (SR-microCT) for DVC are reported. Specimens of cortical and trabecular bovine bone and murine tibiae, were each scanned under zero-strain conditions with an effective voxel size of 1.6 μm. In order to consider the effect of the voxel size, analyses were also performed on downsampled images with voxel size of 8 μm. To evaluate displacement and strain uncertainties, each pair of tomograms was correlated using a global DVC algorithm (ShIRT-FE). Displacement random errors for original SR-microCT ranged from 0.024 to 0.226 μm, depending on DVC nodal spacing. Standard deviation of strain errors was below 200 microstrain (ca. 1/10 of the strain associated with physiological loads) for correlations performed with a measurement spatial resolution better than 40 μm for cortical bovine bone (240 μm for downsampled images), 80 μm for trabecular bovine bone (320 μm for downsampled images) and murine tibiae (120 μm for downsampled images). This study shows that the uncertainties of SR-microCT-based DVC, estimated from repeated scans, are lower than those obtained from LS-microCT-based DVC on similar specimens and low enough to measure accurately the local deformation at the tissue level.

1. Introduction

Musculoskeletal pathologies, such as osteoporosis or bone metastasis, are associated with alterations of bone structures at different spatial scales. Assessment of bone quality (Bouxsein, 2003) and mineral density have become key to studying the effects of pathologies and related treatments at different bone hierarchical levels. Subject-specific computed tomography based finite element (FE) analyses have been used to estimate bone mechanical properties (Dall'Ara et al., 2013; Dall'Ara et al., 2012; Schileo et al., 2008) and the effect of interventions (Keaveny et al., 2014; Zysset et al., 2015) *in vivo*. Combination of FE models and mathematical models of bone remodelling (Lerebours et al., 2015) can estimate bone changes over time. However, first we need to understand how well the structural FE models predict the local 3-dimensional strain field, which can be used to estimate the local cell activity on the bone structural units (Levchuk et al., 2014).

A possible way of validating the FE models at the tissue level is by using digital volume correlation (DVC) (Bay et al., 1999). DVC is a full-field, contactless technique that provides both displacement and strain maps inside bone specimens via the comparison of 3D images acquired in, for example, the unloaded and loaded conditions (Grassi and Isaksson, 2015). DVC approaches based on 'laboratory source' micro-computed tomography (LS-microCT) can measure displacements in bones with sub-voxel accuracy and pre-

* Corresponding author.
E-mail address: e.dallara@sheffield.ac.uk (E. Dall'Ara).

http://dx.doi.org/10.1016/j.jbiomech.2017.04.007
0021-9290/

cision (ca. 1/10–1/20 of the effective voxel size) (Chen et al., 2017; Zauel et al., 2006). However, current LS-microCT-based DVC cannot measure strain in bone with enough precision to validate the model output within a bone structural unit (e.g. a trabecula or an osteon) (Dall'Ara et al., 2014; Roberts et al., 2014). To date, the typical measurement uncertainty enabled using DVC to discriminate the pre- or post-yielding conditions in vertebra bodies scanned with LS-microCT with a voxel size of approximately 35–40 μm (Danesi et al., 2016; Hussein et al., 2012; Tozzi et al., 2016). In fact, as bone yields at a deformation of 7000–10,000 microstrain (Bayraktar et al., 2004), a measurement uncertainty of approximately 700 microstrain could be acceptable for classifying regions starting to yield from those still in the elastic regime. After extensive optimisation, DVC based on LS-microCT has reached acceptable accuracy and precision, on the order of 200 microstrain, but only if a strong compromise with measurement spatial resolution is accepted (measurements every 500–600 μm) (Dall'Ara et al., 2014; Palanca et al., 2015). Unfortunately, due to the heterogeneity of bone tissue, DVC based on LS-microCT cannot be used to obtain accurate measurements of strain within the typical element size of microCT-based FE models (on the order of 10–20 μm).

In order to reduce the strain measurement errors of DVC we can try to improve the input images by, e.g., using synchrotron radiation microCT (SR-microCT). However, it is currently not clear if, and to what extent, better quality tomograms would improve the accuracy of DVC strain measurements. To the authors' knowledge, the only published study that characterised the accuracy of strains computed with DVC based on SR-microCT of bone focused on the crack propagation in murine femora (Christen et al., 2012). However, in that study the precision of the method was assessed only on virtually moved or stretched images, which has been shown to underestimate the real error induced by image noise and artifacts (Dall'Ara et al., 2014). Therefore, the real potential of SR-microCT based DVC for bone applications is still partially unexplored as the potential benefits of using high-quality tomograms that allow resolving micro-features such as osteocyte lacunae are not yet known.

The aim of this study was to quantify the improvement that SR-microCT data could bring to global DVC for different bone tissues, by investigating the compromise between measurement spatial resolution and uncertainties.

2. Materials and methods

2.1. Specimen preparation, tomography and image processing

In order to investigate the effect of microstructure on measurement errors, three different tissue types were used (Fig. 1a–c): four 3 mm in diameter and 12 mm in length cortical bone cores obtained from the diaphysis of a fresh bovine femur (18 months old, killed for alimentary purposes); three 8 mm in diameter and 12 mm in length trabecular bone cores obtained from the greater trochanter of the same femur; and four paired tibiae, which had been used in a previous study (Lu et al., 2015), obtained from two 14-week old female C57BL/6J mice (Harlan Laboratories, Bicester, UK). All machining was performed under constant water irrigation. The soft tissues around the tibiae were carefully removed with a scalpel. All specimens were dehydrated overnight at room temperature and then embedded in acrylic resin without bone infiltration.

Tomography was performed at the Diamond-Manchester Imaging Beamline I13-2 of Diamond Light Source, UK. A filtered (950 μm C, 2 mm Al, 20 μm Ni) polychromatic 'pink' beam (5–35 keV) of parallel geometry was used with an undulator gap of 5 mm. The propagation distance was approximately 10 mm. Tomography data were acquired using a pco.edge 5.5 detector (PCO AG, Germany) coupled to a 750 μm-thick $CdWO_4$ scintillator, with visual optics providing 4× total magnification. This lead to an effective pixel size of 1.6 μm and a field of view of 4.2 × 3.5 mm. 4001 projection images were collected at equally-spaced angles over 180° of continuous rotation, with an exposure time of 53 ms. The total scanning time was approximately four minutes. The projection images were flat and dark corrected prior to reconstruction using the tomographic reconstruction module of Dawn v1.7 (Ashton et al., 2015; Basham et al., 2015), which incorporated ring artefact suppression (Titarenko et al., 2010). Samples were mounted such that their long axes corresponded to the rotation axis during data collection. Each specimen was scanned twice under zero-strain conditions and without any repositioning.

Two cubic volumes of interest (VOIs), with side lengths of 1000 voxels, were cropped from the middle of each cortical and trabecular specimen (Fig. 1d, e, g, h) using ImageJ-v1.49 (Rasband, NIH, Maryland, USA, http://imagej.nih.gov/ij/). In order to include both trabecular and cortical bone, one cubic VOI (Fig. 1f, i) was cropped from the proximal part of each murine tibia.

In order to allow comparison between the results obtained from other DVC approaches, the image datasets used in the present study are available by contacting the corresponding author (results can be found at https://doi.org/10.15131/shef.data.4865300). .

In order to evaluate the DVC errors only where bone tissue is present, masked images were created: after applying a Gaussian filter ($\sigma = 4$) to reduce high-frequency noise, image segmentation was performed, followed by a single-level threshold in the valley between the first two peaks of the greyscale histogram. The threshold was adjusted visually by comparing the segmented and greyscale images. These binary images (0 for background, 1 for bone voxels) were then used also to mask the original bovine trabecular bone and murine tibia VOIs (Fig. 1j, k).

For each VOI the solid volume fraction (solid volume/total volume, SV/TV), was determined as the ratio between the number of bone voxels and the total number of voxels in the VOI, using the ImageJ plug-in BoneJ (Doube et al., 2010).

The potential benefit associated with SR-microCT could be due both to the signal-to-noise ratio and the voxel size. In order to evaluate the effect of the voxel size on the strain uncertainties, all original (not masked) VOIs were downsampled to a voxel size of 8 μm (by averaging the voxels grey-values) using ImageJ. With a similar approach, downsampled binary masks were created from the original masks for trabecular bone and murine tibiae and assigning 1 to any value greater than 0.

2.2. DVC protocol

The adopted DVC approach (ShIRT-FE) was a combination of a global deformable image registration algorithm (Sheffield Image Registration toolkit, ShIRT (Barber and Hose, 2005; Barber et al., 2007)) that computes the displacements maps, and a finite element (FE) software package for the calculation and visualization of the strains (Dall'Ara et al., 2014; Palanca et al., 2015; Palanca et al., 2016; Tozzi et al., 2017). Briefly, a grid with selectable nodal spacing (NS) was superimposed on the VOIs from pairs of repeated scans. ShIRT computes the displacements at the nodes of the grid by solving the registration equation (Barber and Hose, 2005; Barber et al., 2007). The grid is then converted into 8-nodes hexahedral FE mesh, the computed displacements are assigned as boundary conditions (Fig. 2), the FE software package is used to differentiate the displacement field (ANSYS Mechanical APDL v. 15.0, Ansys, Inc., USA), and the six components of strain are computed at each node. As it has been demonstrated that nodal spacing (NS) affects uncertainties of the method (Dall'Ara et al., 2014), a series of NS values was used (from 10 to 300 voxels, equivalent to 16.0–480.0 μm) for every pair of repeated tomograms (Table 1).

For the bovine trabecular bone and murine tibia samples, which showed lower SV/TV than the bovine cortical samples (approximately 96% for cortical bone versus approximately 26% for trabecular bone and murine tibia, Fig. 1), two approaches were taken in order to investigate the effect of the inclusion of the marrow regions during the registration: either the whole VOI ('unmasked'), or only the parts of the VOI within the mask ('masked') were registered. In both cases (unmasked and masked) the cells of the mesh with all nodes outside the mask were ignored and the errors were averaged only in the remaining nodes (Fig. 2), in order to account only for the errors within the bone tissue. The same protocol was applied also to the downsampled images using the downsampled masks.

2.3. Quantification of errors

The systematic error for the displacements could not be quantified, due to unknown nano-movements of the moving parts of the scanner. Conversely, as the test was based on a zero-strain condition, any non-zero values of strain were considered as error, and both precision and accuracy could be estimated. The following parameters were computed for each registration:

- Random error for the displacement: standard deviation (SD) of each component of displacement, as in (Benoit et al., 2009; Madi et al., 2013; Palanca et al., 2015; Roux et al., 2008);
- Mean absolute error (MAER): average of the average of the absolute values of the six components of strain in each node, referred as "accuracy" in (Liu and Morgan, 2007);
- Standard deviation of error (SDER): SD of the average of the absolute values of the six components of strain in each node, referred as "precision" in (Liu and Morgan, 2007);
- Systematic error for each component of strain: average of the respective component of strain on the evaluated nodes, as in (Gillard et al., 2014; Palanca et al., 2016);
- Random error for each component of strain: SD of the respective component of strain on the evaluated nodes, as in (Gillard et al., 2014; Palanca et al., 2016);

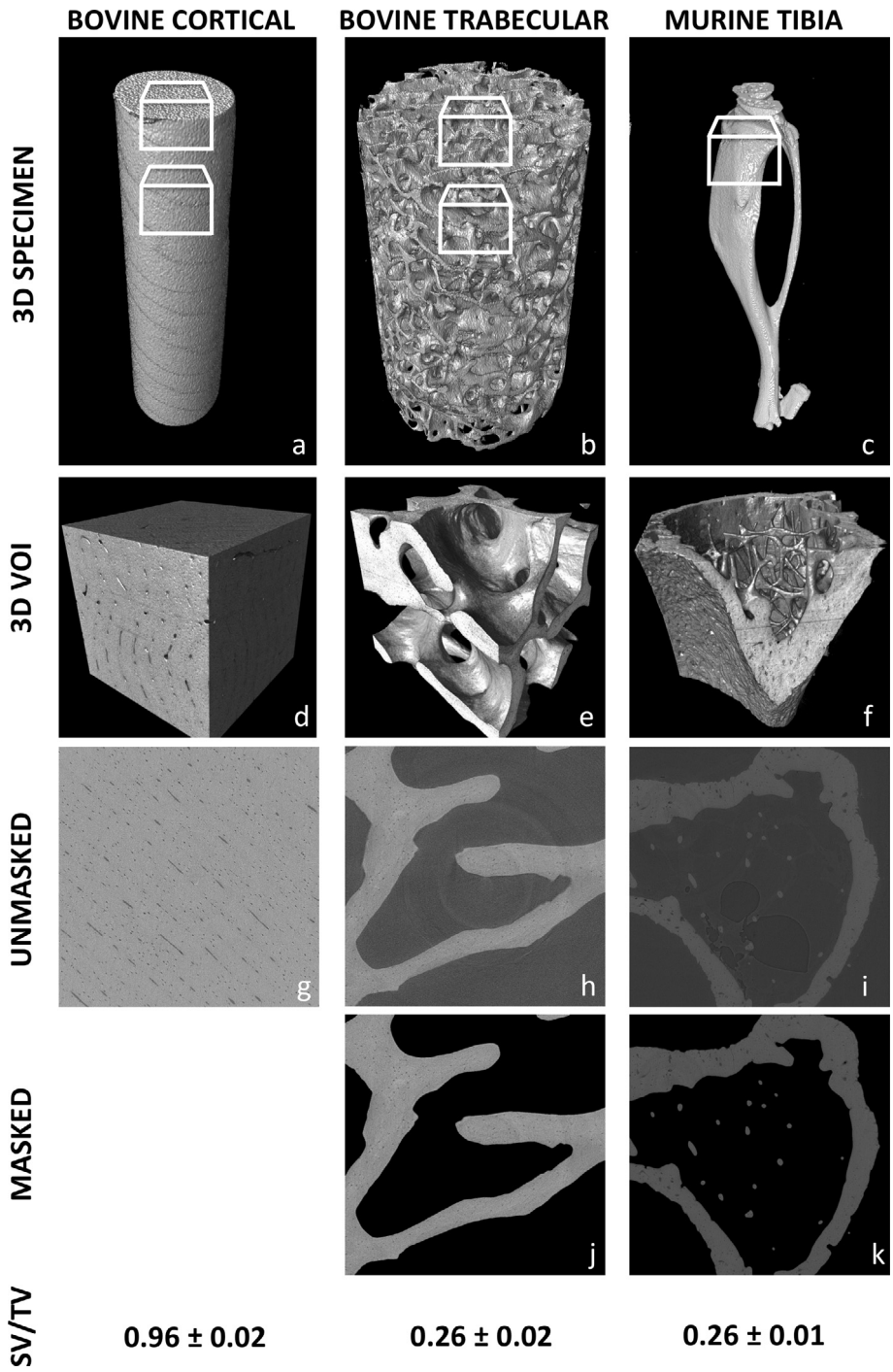

Fig. 1. Typical specimen for each tissue type. From top to bottom: 3-dimensional (3D) representation of a typical specimen; 3D representation of typical VOI; 2-dimensional (2D) cross-section through the middle of each VOI; masked 2D cross-sections; solid volume fraction (SV/TV) values (median ± standard deviation). The side length of each cross section is 1000 voxels, equivalent to 1600 μm.

The median and standard deviation were computed within each sample for such errors.

3. Results

3.1. Random error for the displacements

The random errors of each component of the displacement, obtained using the registration based on the unmasked images never exceeded 0.139 voxels (0.226 μm; for trabecular bone with a NS of 10, Table 2). The maximal random errors, obtained at NS equal to 10, were smallest for the bovine cortical sample (below 0.054 voxels for z-direction, 0.088 μm), followed by the ones for the murine tibia sample (below 0.080 voxels for x-direction, 0.130 μm), and largest for the ones computed for bovine trabecular sample (below 0.139 voxels for z-direction, 0.226 μm). The errors obtained for the displacements using the masked images were lower than those for the unmasked images for both bovine trabecular bone and murine tibia samples (Table 2). A trend could be observed for all bone types: the higher the NS, the lower the random error. No preferential direction was observed.

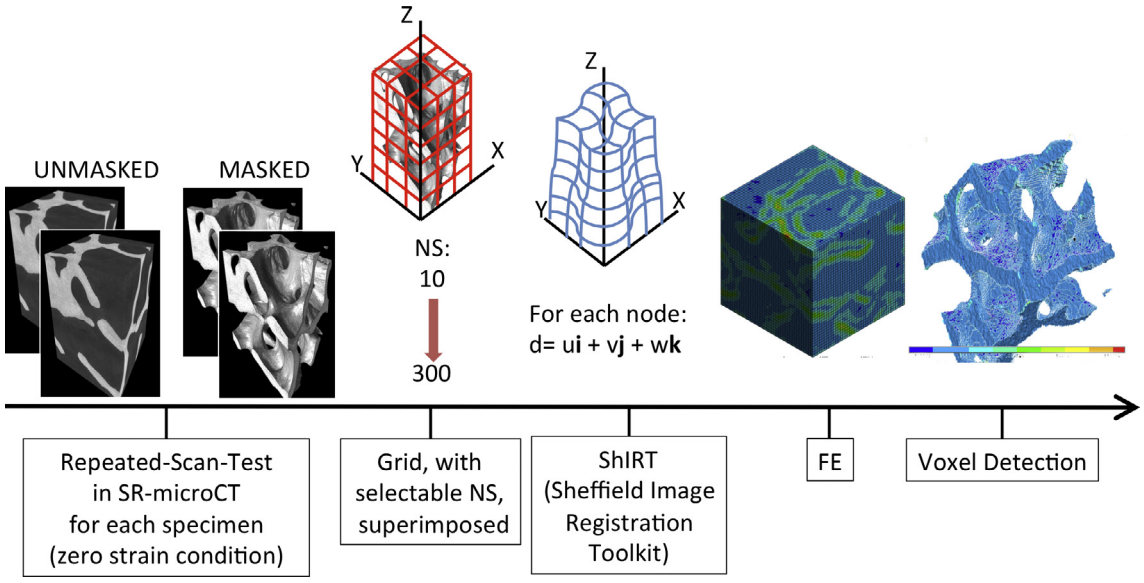

Fig. 2. Workflow of the registration procedure. Tomograms were obtained by scanning the specimens twice without any repositioning. From left to right: a grid of particular nodal spacing (NS, from 10 to 300 voxels) was superimposed on the cropped VOIs (unmasked or masked, in case of trabecular and murine tibiae); the displacements were evaluated at each node by ShIRT; the grid was converted to an FE mesh and computed displacements assigned as boundary conditions; the cells of the grid with all nodes outside the mask were ignored when evaluating measurement uncertainties.

Table 1
List of investigated nodal spacings and nominal numbers of elements and nodes inside the VOI. Finer steps were used for lower NS (10–25 voxels) and coarser steps for higher NS (50–300 voxels).

Nodal spacing (voxels)	Nodal spacing (μm)	Nominal number of elements inside VOI	Nominal number of nodes inside VOI
10	16.0	1,000,000	1,030,301
15	24.0	314,432	328,509
20	32.0	125,000	132,651
25	40.0	64,000	68,921
50	80.0	8,000	9,261
75	120.0	2,744	3,375
100	160.0	1,000	1,331
150	240.0	512	729
200	320.0	216	343
250	400.0	64	125
300	480.0	64	125

3.2. Accuracy and precision: average of components

As expected from the results reported in previous studies on bone (Benoit et al., 2009; Dall'Ara et al., 2014; Palanca et al., 2016) and on polypropylene-foam (Roux et al., 2008), the uncertainties of the DVC approach (MAER and SDER) had decreasing trends with respect to NS, for all types of bone (Fig. 3). For a given NS, the values of MAER were larger than SDER.

The ranges (for NS of 16.0–480.0 μm) of the medians for MAER and SDER for bovine cortical bone sample were between 29–2026 microstrain and between 8–890 microstrain, respectively. Errors for this bone type were lower than those obtained for the other types of bone (from registration based on masked or unmasked images). For bovine trabecular bone the MAER ranged between 49–4058 microstrain and 41–1795 microstrain for unmasked and masked images, respectively. For murine tibiae the MAER ranged between 43–3868 microstrain and 51–1394 microstrain for unmasked and masked images, respectively. Lower SDER was found for the bovine trabecular bone (between 17–2253 micros-

Table 2
Random errors for the components of displacement (μm) for each bone type.

Ns	Displacement random errors (μm)														
	Bovine cortical			Bovine trabecular unmasked			Bovine trabecular masked			Murine tibia unmasked			Murine tibia masked		
	X	Y	Z	X	Y	Z	X	Y	Z	X	Y	Z	X	Y	Z
10	0.073	0.072	0.088	0.171	0.176	0.226	0.108	0.101	0.152	0.130	0.118	0.118	0.103	0.087	0.084
15	0.053	0.049	0.069	0.143	0.143	0.192	0.095	0.092	0.133	0.093	0.078	0.079	0.099	0.081	0.078
20	0.051	0.046	0.067	0.139	0.141	0.201	0.090	0.083	0.128	0.089	0.074	0.081	0.094	0.077	0.072
25	0.047	0.041	0.061	0.123	0.125	0.186	0.086	0.077	0.116	0.085	0.072	0.078	0.092	0.076	0.070
50	0.039	0.033	0.058	0.087	0.091	0.156	0.068	0.064	0.102	0.074	0.061	0.066	0.085	0.071	0.059
75	0.036	0.032	0.061	0.075	0.081	0.144	0.056	0.057	0.098	0.070	0.057	0.061	0.083	0.069	0.052
100	0.033	0.027	0.055	0.056	0.062	0.114	0.043	0.051	0.086	0.067	0.054	0.053	0.082	0.068	0.049
150	0.031	0.029	0.060	0.047	0.053	0.096	0.037	0.045	0.079	0.062	0.051	0.045	0.075	0.071	0.047
200	0.029	0.025	0.055	0.038	0.041	0.084	0.031	0.042	0.076	0.057	0.050	0.041	0.076	0.071	0.045
250	0.034	0.038	0.068	0.050	0.056	0.103	0.037	0.042	0.062	0.055	0.043	0.057	0.068	0.065	0.040
300	0.024	0.026	0.053	0.030	0.030	0.061	0.027	0.034	0.056	0.049	0.039	0.033	0.065	0.063	0.038

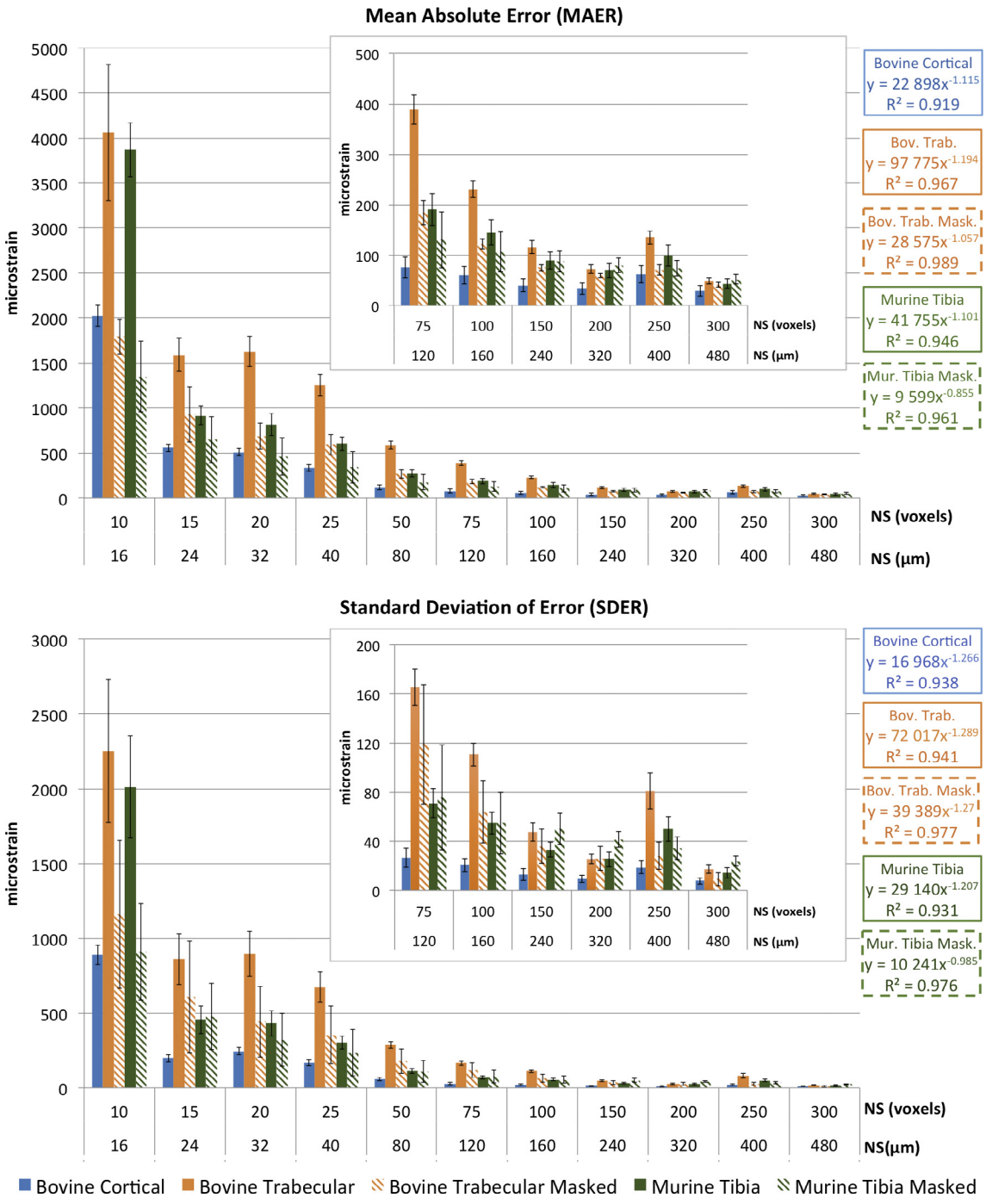

Fig. 3. MAER (top) and SDER (bottom) for each bone type (bovine cortical bone in blue, bovine trabecular bone in orange and murine tibia in green), for unmasked and masked images (solid and striped bars, respectively) as a function of the nodal spacing NS. Bars represent the median values, while error bars represent the standard deviation. On the right, the power laws and the coefficients of determination (R^2) are reported. (For interpretation of the references to colour in this figure legend, the reader is referred to the web version of this article.)

train and 9–1162 microstrain for unmasked and masked images) and for the murine tibia sample (between 14–2012 and 24–909 microstrain for unmasked and masked images).

Downsampling the images increased the median errors for all bone types for both MAER (113–11971 microstrain for cortical bone, 265–14650 microstrain for trabecular bone and 86–7011 microstrain for murine tibiae) and SDER (36–4790 microstrain for cortical bone, 124–8985 microstrain for trabecular bone and 19–4165 microstrain for murine tibiae). The power laws for MAER and SDER showed similar trends but different amplitude for native resolution, downsampled images and LS-microCT images of similar samples (Dall'Ara et al., 2014) (Fig. 4).

3.3. Systematic errors for each component of strain

The systematic errors were independent from NS, for all bone types and for both registrations based on unmasked or masked images (Fig. Sup.1 in Supplementary Material). Only weak reductions of the systematic errors for the normal components have been observed for mouse tibiae for both unmasked and masked

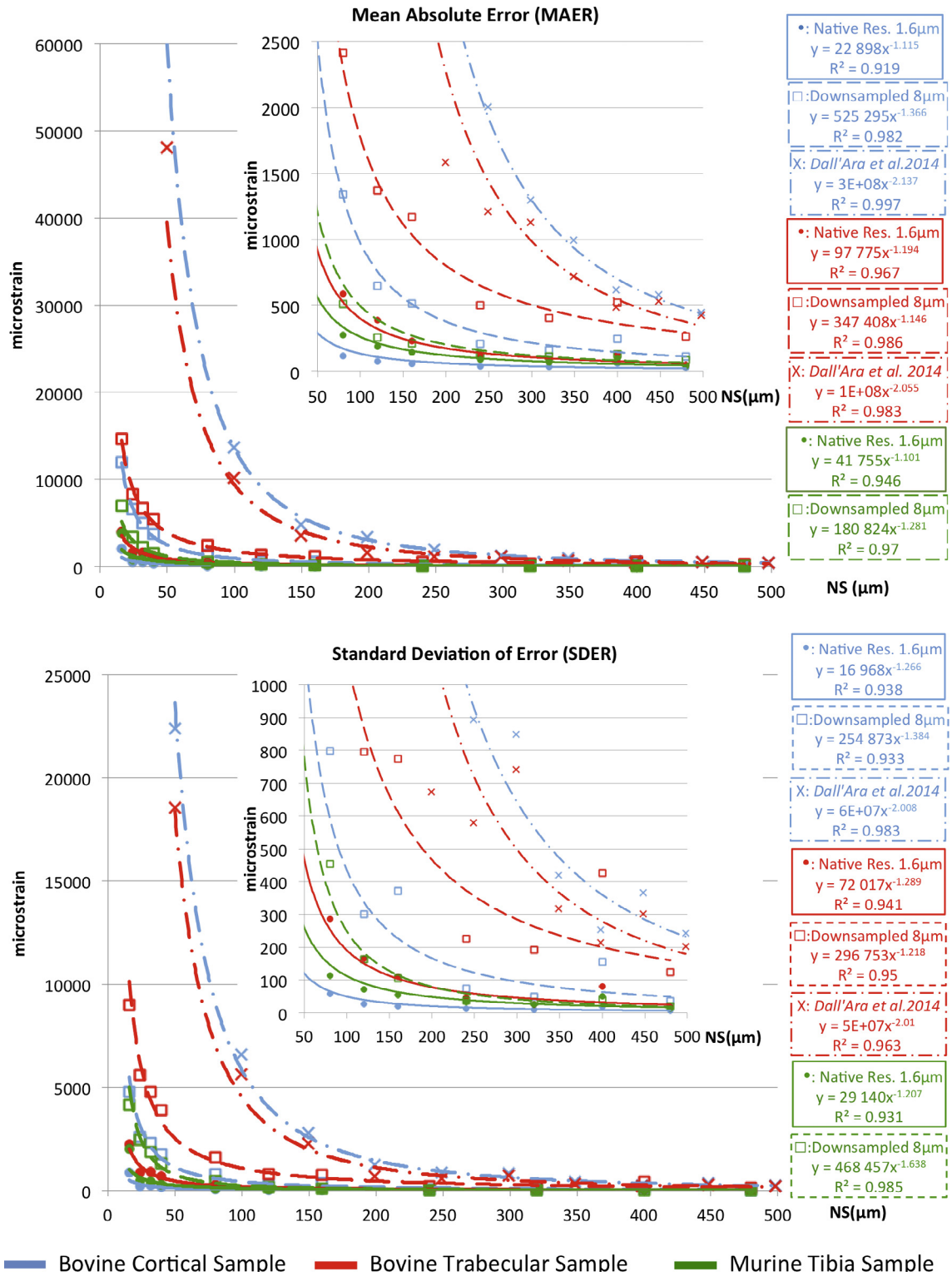

Fig. 4. Medians and power laws computed for MAER (top) and SDER (bottom) for each bone type (bovine cortical bone in blue, bovine trabecular bone in orange and murine tibia in green), for native SR-microCT images (solid lines), downsampled SR-microCT images (dashed lines) and LS-microCT images from Dall'Ara et al. (2014) (dash-dot lines). On the right, the power laws and the coefficients of determination (R^2) are reported. (For interpretation of the references to colour in this figure legend, the reader is referred to the web version of this article.)

images. The medians of the systematic errors for the bovine cortical bone sample ranged between −43 and 80 microstrain, and were lower than those of the other two bone types (between −55 and 124 microstrain and between −133 and 88 microstrain for bovine trabecular bone with unmasked and masked images, respectively; between −17 and 197 microstrain and between −6 and 209 microstrain for murine tibiae using unmasked and masked images, respectively). In most cases no systematic preferential direction

was observed. Larger errors were found for normal components in the mouse tibiae. The downsampled images confirmed the independence of the systematic errors from the NS, but showed higher values errors (between −74 and 264 microstrain for the bovine cortical bone, between −207 and 590 for the bovine trabecular bone, and between −12 and 219 for the murine tibiae).

3.4. Random errors for each component of strain

For all registrations, increasing the NS reduced the random error for each component of strain (Fig. 5). As observed for the displacement, bovine cortical bone showed the lowest random errors, with medians ranging between 14 and 3271 microstrain. Bovine trabecular bone was associated to random errors of 32–7480 and 23–3228 microstrain using unmasked images, and masked images, respectively. The murine tibiae showed errors of 23–6669 and 23–2543 microstrain using unmasked and masked images, respectively. Random errors were largest for the shear strains in all cases (approximately 1.5 times higher than for the normal strain). The same trend was observed for the downsampled images. Here, the murine tibiae had the lowest random errors (57–12,051 microstrain). The bovine cortical bone had errors between 77 and 18,810 microstrain and the bovine trabecular bone between 249 and 25,185 microstrain.

3.5. Spatial distribution of the errors

The distribution of the apparent normal strain along the z-direction varied between bone types, and even more pronouncedly with the NS (Fig. 6). Having applied the DVC to repeated images of the same undeformed specimens (zero-strain condition), this strain represents the error distribution within each bone structure.

For bovine cortical bone, a reasonably uniform strain distribution was obtained with NS equal to 50 and 100 voxels (80 and 160 μm). Conversely, for the bovine trabecular bone and murine tibiae, the bone surface and those regions with limited number of features within the volume (e.g. central portion of the murine tibia) showed larger strain errors. It must be noted that for trabecular bone with NS equal to 50 voxels (80 μm) the peak errors were in most cases in regions outside the bone or close to the border of the image.

4. Discussion

The potential of DVC for bone applications is still partially unexplored, as this approach has not been yet applied intensively to high-quality images. In this study measurement uncertainties of a SR-microCT based DVC approach were evaluated for the first time for three different types of bone by using Repeated-Scan-Tests (Palanca et al., 2015).

In line with previous studies performed on LS-microCT images (Dall'Ara et al., 2014; Palanca et al., 2015; Palanca et al., 2016; Tozzi et al., 2017), also for DVC based on SR-microCT, the larger the NS the lower the measurement uncertainties. This trend is probably due to the fact that even for higher image quality, the displacement errors were only modestly affected by the NS (e.g. for NS 10 and 100 voxels, the random error was reduced by a factor 2 if the NS was increased by a factor 10, Table 1), which lead to increased strain errors for smallest distance between the nodes of the grid.

For the bovine trabecular bone, registrations based on masked images showed lower errors compared to the ones obtained by registering unmasked images. This finding highlights how the exclusion of low-contrast marrow regions, for which noise and artefacts probably dominate the registration, is beneficial for DVC. Conversely for murine tibiae the SDERs computed with unmasked or masked images were similar for NSs larger than 10 voxels (16 μm). This different effect of the masking could be due to differences in size and shape of the bone features that form the two microstructures.

This study explored the relationships between spatial resolution of the DVC strain measurements and the associated error for the different bone types. Not surprisingly, the trend of the DVC uncertainties followed a power law for all bone types, confirming what was previously found for LS-microCT based bone specimens (Dall'Ara et al., 2014; Roberts et al., 2014) or for polypropylene-foam specimens (Roux et al., 2008). For NSs of 40 μm or larger, the SDER for the cortical bone images were lower than 200 microstrain, acceptable error when investigating deformations in the physiological range. For registrations using the masked images, median SDER values lower than 200 microstrain were found for NS larger than 80 μm for the murine tibiae, or larger than 120 μm for the bovine trabecular bone. Larger NSs were required to reduce the error associated to each component of strain below 200 microstrain (80 μm for the cortical bone, 160 μm for masked trabecular bone, and 120 μm for masked murine tibiae). These values are acceptable for measurements performed on bone structural units, and suggest that the SR-microCT based DVC can be used to validate computational models that aim to predict local strains at the tissue level (Chen et al., 2017; Eswaran et al., 2007; Van Rietbergen et al., 1995; Verhulp et al., 2006).

In the present study the errors were vastly lower than those obtained processing traditional LS-microCT (voxel size of ~10 μm) images (Dall'Ara et al., 2014) of similar specimens from the same femur processed in this study, using the same DVC approach on Repeated-Scan-Tests. In that study, SDER below 200 microstrain were achieved only for NS above 472 μm for trabecular bone, and 536 μm for cortical bone. The present study proved that the DVC uncertainties could be reduced, improving the measurement spatial resolution almost fourteen times for cortical bone and almost four times for trabecular bone. This difference could be due to the superimposition of two effects in the SR-microCT images: the smaller effective voxel size and the higher signal-to-noise ratio. When the downsampled images were analysed, SDER of 200 microstrain were achieved with a measurement spatial resolution of 176 μm for the cortical bone (five times coarser than the 34 μm needed for the original images), and of 402 μm for the trabecular bone (four times coarser than the 97 of the original images). These analyses showed that a finer voxel size can explain only partially the lower SDER of the DVC with SR-microCT. Such measurement spatial resolutions were still better than those required to obtain the same SDER with LS-microCT (Dall'Ara et al., 2014). The larger improvement for cortical bone is likely due to the much higher number of features (i.e. the osteocyte lacunae around the vascular pores) resolvable with SR-microCT images for such microstructure compared to LS-microCT images. However, as comparisons were made between SR-microCT and LS-microCT images of similar (but not identical) specimens, further investigations could help to better clarify the sources of errors.

All the above-mentioned considerations were based on analyses of data from zero-strain tests. While a detailed analyses of DVC precision under loading will need a more comprehensive future study for estimating the effect of loading condition, loading direction and loading level for different structures, in this manuscript we report some preliminary results obtained from virtually compressed cortical specimens (Section S2 in Supplementary Material).

To the authors' knowledge, this is the first study where the displacement and strain errors of a global DVC approach based on SR-microCT images were evaluated with Repeated-Scan-Tests and virtually compressed repeated images for different types of bone specimens. Another study used synchrotron images on a

Sample	Bovine Cortical	Bovine Trabecular	Murine Tibia
Nr specimens	4	3	4
Nr VOIs	8	6	4
Masked	✗	✔	✔

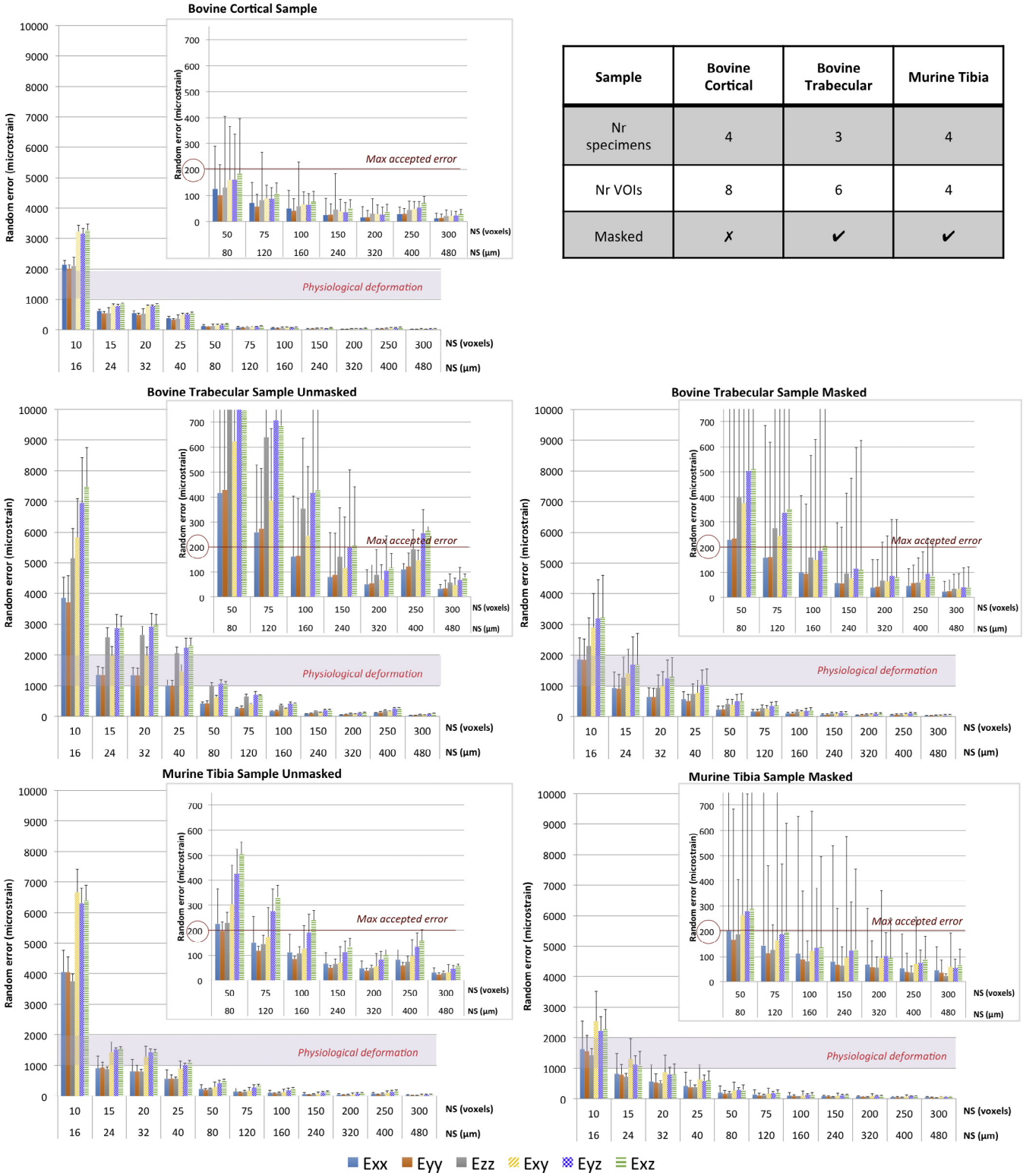

Fig. 5. Median of the random error for each bone type (cortical bone on the top, trabecular bone in the middle and murine tibiae on the bottom), for each registration methods (from unmasked images on the left, from masked images on the right), for each component of strain, as a function of NS. To improve the readability, error bars representing standard deviations were reported only on the top of each histogram. To help interpreting the results, a range for the typical physiological deformations (1,000–2,000 microstrain Yang., et al., 2011) is indicated. For the scope of this study, also the target value for the measurement error is indicated (one order of magnitude lower: 200 microstrain).

DVC approach and performed a preliminary evaluation of the error (Christen et al., 2012) on virtually moved and stretched images of murine femur. That DVC approach, based on demons deformable registration algorithm, was applied to SR-microCT images (voxel size of 740 nm) with a NS of approximately 30 µm and provided SDER of approximately 1800 microstrain, more than four times lar-

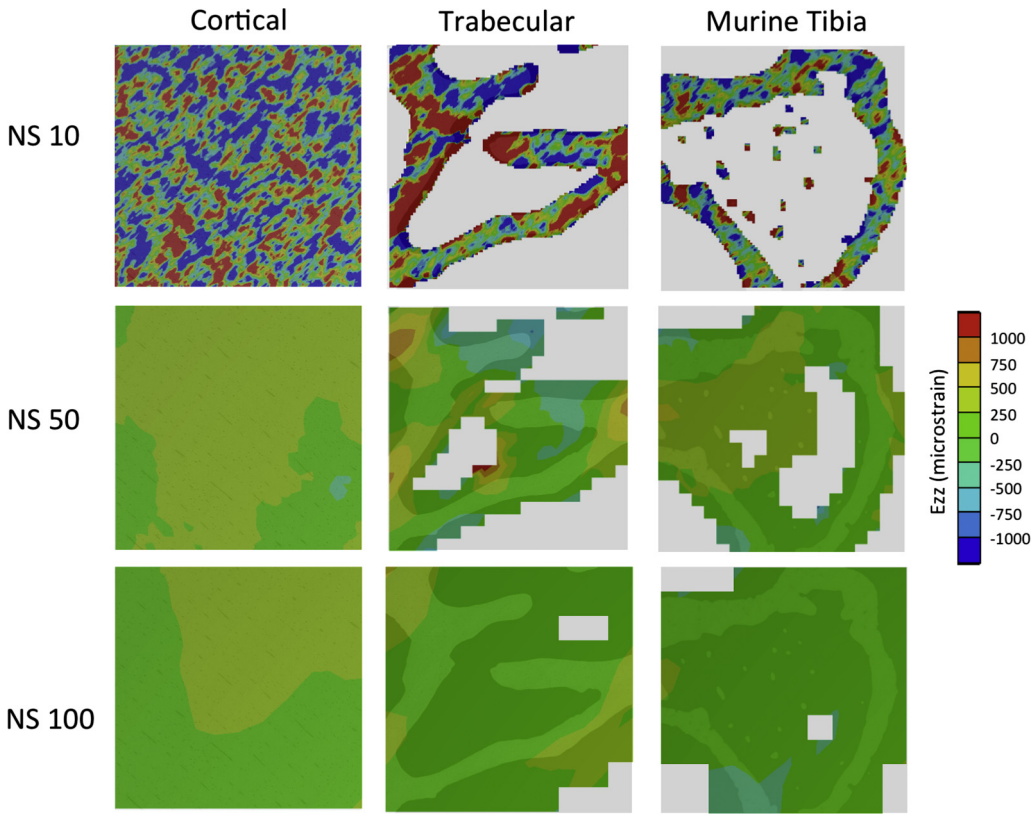

Fig. 6. Distribution of z-direction normal strain shown for a mid-height cross-section for a typical specimen of each bone type for three nodal spacing (10, 50, 100). For trabecular bone and murine tibiae the masked images were used for this analyses. As the DVC was applied to repeated images of the same undeformed specimens, the reported strain represents in fact the DVC measurement uncertainties. The cross-section image of the corresponding slice was overlapped to the strain error map. For every microstructure, the side length of the image is 1,600 μm.

ger than that found for masked murine tibiae in this study. This difference might be due to differences in microstructure, tomographic resolution and registration method. However, considering that in that study the SDER was computed on virtually moved images that do not include the effect of image noise, the method proposed in this study is by far the one with the highest precision (lowest SDER) reported in the literature to date for analyses on bone specimens. It remains to be investigated if other DVC approaches would achieve similar (or better) precision if based on the same images used in the present study.

Despite the high potential of SR-microCT based DVC, bone damage induced by X-ray synchrotron irradiation is apparently the major limitation for its application in time-lapsed *in situ* mechanical tests (Barth et al., 2010). Previous authors have attempted to mechanically test bone samples within a synchrotron facility (Christen et al., 2012; Thurner et al., 2006) but reported that the irradiation and/or associated heat affected the local material properties of the tissue (Barth et al., 2010). In order to apply this DVC approach to SR-microCT *in situ* mechanically tested and imaged bone samples further scanning optimization (Pacureanu et al., 2012) and analysis to reduce this problem by, for example, reducing exposure times, supressing lower X-ray frequencies or submerging samples in aqueous buffer, would form the basis of a useful methodological study.

The main limitation of this study is that the measurement uncertainties were investigated in a homogeneous zero-strain case. It would be interesting to further study the evolution of errors within strained specimens, especially where the gradients of strains are highest. Moreover, the error associated to the strain and displacement measurements was evaluated for a global DVC approach. While similar trends can be expected also for local DVC approaches (Leclerc et al., 2012; Palanca et al., 2015) researchers are welcome to download the images used in this study for comparing different methods.

5. Conclusion

The uncertainties associated with a global DVC approach applied to Synchrotron tomograms with small voxel size are sufficiently low to allow reliable strain measurements at the tissue-level in different bone structures. This method can be used to evaluate local bone deformations under loading, and to validate the strain predicted by computational models at the tissue-level.

Conflict of interest

Authors have no conflict of interest associated to this paper.

Acknowledgments

The authors would like to acknowledge Yuan Chen, Andre Castro, Ana Campos-Marin, Claudia Wittkowske, Luke Boldock and Kazimir Wanelik for help during experiments at Diamond Light Source. We acknowledge Diamond Light Source for time at the Diamond-Manchester Imaging Beamline I13-2, under proposal MT10315. This study was partially funded by the FP7 European program MAMBO (PIEF-GA-2012-327357) and by the EPSRC Frontier Grant Multisim (EP/K03877X/1). Palanca acknowledges the 'Marco Polo' travel grant awarded by University of Bologna.

Appendix A. Supplementary material

Supplementary data associated with this article can be found, in the online version, at http://dx.doi.org/10.1016/j.jbiomech.2017.04.007.

References

Ashton, A.W., Aishima, J., Basham, M., Chang, P., El Kassaby, B., Filik, J., Gerring, M., Levik, K., Sikharulidze, I., Webber, M., Wharmby, M.T., 2015. Dawn Science v1.7 (DLS Edition).p.

Barber, D.C., Hose, D.R., 2005. Automatic segmentation of medical images using image registration: diagnostic and simulation applications. J. Med. Eng. Tech. 29, 53–63.

Barber, D.C., Oubel, E., Frangi, A.F., Hose, D.R., 2007. Efficient computational fluid dynamics mesh generation by image registration. Med. Image Anal. 11, 648–662.

Barth, H.D., Launey, M.E., Macdowell, A.A., Ager 3rd, J.W., Ritchie, R.O., 2010. On the effect of X-ray irradiation on the deformation and fracture behavior of human cortical bone. Bone 46, 1475–1485.

Basham, M., Filik, J., Wharmby, M.T., Chang, P.C., El Kassaby, B., Gerring, M., Aishima, J., Levik, K., Pulford, B.C., Sikharulidze, I., Sneddon, D., Webber, M., Dhesi, S.S., Maccherozzi, F., Svensson, O., Brockhauser, S., Naray, G., Ashton, A.W., 2015. Data analysis WorkbeNch (DAWN). J. Synchrotron Radiat. 22, 853–858.

Bay, B.K., Smith, T.S., Fyhrie, D.P., Saad, M., 1999. Digital volume correlation: three-dimensional strain mapping using X-ray tomography. Exp. Mech. 39, 217–226.

Bayraktar, H.H., Morgan, E.F., Niebur, G.L., Morris, G.E., Wong, E.K., Keaveny, T.M., 2004. Comparison of the elastic and yield properties of human femoral trabecular and cortical bone tissue. J. Biomech. 37, 27–35.

Benoit, A., Guerard, S., Gillet, B., Guillot, G., Hild, F., Mitton, D., Perie, J.N., Roux, S., 2009. 3D analysis from micro-MRI during in situ compression on cancellous bone. J. Biomech. 42, 2381–2386.

Bouxsein, M.L., 2003. Bone quality: where do we go from here? Osteoporos. Int. 14 (Suppl. 5), S118–S127.

Chen, Y., Dall'Ara, E., Sales, E., Manda, K., Wallace, R., Pankaj, P., Viceconti, M., 2017. Micro-CT based finite element models of cancellous bone predict accurately displacement once the boundary condition is well replicated: A validation study. J. Mech. Behavior Biomed. Mater. 65, 644–651.

Christen, D., Levchuk, A., Schori, S., Schneider, P., Boyd, S.K., Muller, R., 2012. Deformable image registration and 3D strain mapping for the quantitative assessment of cortical bone microdamage. J. Mech. Behavior Biomed. Mater. 8, 184–193.

Dall'Ara, E., Barber, D., Viceconti, M., 2014. About the inevitable compromise between spatial resolution and accuracy of strain measurement for bone tissue: a 3D zero-strain study. J. Biomech. 47, 2956–2963.

Dall'Ara, E., Luisier, B., Schmidt, R., Kainberger, F., Zysset, P., Pahr, D., 2013. A nonlinear QCT-based finite element model validation study for the human femur tested in two configurations in vitro. Bone 52, 27–38.

Dall'Ara, E., Pahr, D., Varga, P., Kainberger, F., Zysset, P., 2012. QCT-based finite element models predict human vertebral strength in vitro significantly better than simulated DEXA. Osteoporos. Int. 23, 563–572.

Danesi, V., Tozzi, G., Cristofolini, L., 2016. Application of digital volume correlation to study the efficacy of prophylactic vertebral augmentation. Clin. Biomech. 39, 14–24.

Doube, M., Klosowski, M.M., Arganda-Carreras, I., Cordelieres, F., Dougherty, R.P., Jackson, J., Schmid, B., Hutchinson, J., Shefelbine, S., 2010. BoneJ: free and extensible bone image analysis in ImageJ. Bone 47, 1076–1079.

Eswaran, S.K., Gupta, A., Keaveny, T.M., 2007. Locations of bone tissue at high risk of initial failure during compressive loading of the human vertebral body. Bone 41, 733–739.

Gillard, F., Boardman, R., Mavrogordato, M., Hollis, D., Sinclair, I., Pierron, F., Browne, M., 2014. The application of digital volume correlation (DVC) to study the microstructural behaviour of trabecular bone during compression. J. Mech. Behav. Biomed. Mater. 29, 480–499.

Grassi, L., Isaksson, H., 2015. Extracting accurate strain measurements in bone mechanics: a critical review of current methods. J. Mech. Behav. Biomed. Mater. 50, 43–54.

Hussein, A.I., Barbone, P.E., Morgan, E.F., 2012. Digital volume correlation for study of the mechanics of whole bones. Procedia IUTAM 4, 116–125.

Keaveny, T.M., McClung, M.R., Genant, H.K., Zanchetta, J.R., Kendler, D., Brown, J.P., Goemaere, S., Recknor, C., Brandi, M.L., Eastell, R., Kopperdahl, D.L., Engelke, K., Fuerst, Radcliffe, H.S., Libanati, C., 2014. Femoral and vertebral strength improvements in postmenopausal women with osteoporosis treated with denosumab. J. Bone Miner. Res. 29, 158–165.

Leclerc, H., Perle, J.N., Hild, F., Roux, S., 2012. Digital volume correlation: what are the limits to the spatial resolution? Mech. Ind. 13, 361–371.

Lerebours, C., Buenzli, P.R., Scheiner, S., Pivonka, P., 2015. A multiscale mechanobiological model of bone remodelling predicts site-specific bone loss in the femur during osteoporosis and mechanical disuse. Biomech. Model. Mechanobiol. 15, 1.

Levchuk, A., Zwahlen, A., Weigt, C., Lambers, F.M., Badilatti, S.D., Schulte, F.A., Kuhn, G., Muller, R., 2014. The Clinical Biomechanics Award 2012 - presented by the European Society of Biomechanics: large scale simulations of trabecular bone adaptation to loading and treatment. Clin. Biomech. 29, 355–362.

Liu, L., Morgan, E.F., 2007. Accuracy and precision of digital volume correlation in quantifying displacements and strains in trabecular bone. J. Biomech. 40, 3516–3520.

Lu, Y., Boudiffa, M., Dall'Ara, E., Bellantuono, I., Viceconti, M., 2015. Evaluation of in-vivo measurement errors associated with micro-computed tomography scans by means of the bone surface distance approach. Med. Eng. Phys. 37, 1091–1097.

Madi, K., Tozzi, G., Zhang, Q.H., Tong, J., Cossey, A., Au, A., Hollis, D., Hild, F., 2013. Computation of full-field displacements in a scaffold implant using digital volume correlation and finite element analysis. Med. Eng. Phys. 35, 1298–1312.

Pacureanu, A., Langer, M., Boller, E., Tafforeau, P., Peyrin, F., 2012. Nanoscale imaging of the bone cell network with synchrotron X-ray tomography: optimization of acquisition setup. Med. Phys. 39, 2229–2238.

Palanca, M., Tozzi, G., Cristofolini, L., Viceconti, M., Dall'Ara, E., 2015. 3D local measurements of bone strain and displacement: comparison of three digital volume correlation approaches. J. Biomech. Eng. (ASME) 137. 071006-071001/071006-071014.

Palanca, M., Tozzi, G., Dall'Ara, E., Curto, M., Innocente, F., Danesi, V., Cristofolini, L., 2016. Digital Volume Correlation can be used to estimate local strains in natural and augmented vertebrae: an organ-level study. J. Biomech. 49, 3882–3890.

Roberts, B.C., Perilli, E., Reynolds, K.J., 2014. Application of the digital volume correlation technique for the measurement of displacement and strain fields in bone: a literature review. J. Biomech. 47, 923–934.

Roux, S., Hild, F., Viot, P., Bernard, D., 2008. Three-dimensional image correlation from X-ray computed tomography of solid foam. Compos. A Appl. Sci. Manuf. 39, 1253–1265.

Schileo, E., Dall'ara, E., Taddei, F., Malandrino, A., Schotkamp, T., Baleani, M., Viceconti, M., 2008. An accurate estimation of bone density improves the accuracy of subject-specific finite element models. J. Biomech. 41, 2483–2491.

Thurner, P.J., Wyss, P., Voide, R., Stauber, M., Stampanoni, M., Sennhauser, U., Müller, R., 2006. Time-lapsed investigation of three-dimensional failure and damage accumulation in trabecular bone using synchrotron light. Bone 39, 289–299.

Titarenko, S., Withers, P.J., Yagola, A., 2010. An analytical formula for ring artefact suppression in X-ray tomography. Appl. Math. Lett. 23, 1489–1495.

Tozzi, G., Dall'Ara, E., Palanca, M., Curto, M., Innocente, F., Cristofolini, L., 2017. Strain uncertainties from two DVC approaches in prophylactically augmented vertebrae: local analysis on bone and bone-cement microstructures. J. Mech. Behavior Biomed. Mater. 67, 117–126.

Tozzi, G., Danesi, V., Palanca, M., Cristofolini, L., 2016. Elastic full-field strain analysis and microdamage progression in the vertebral body from digital volume correlation. Strain 52, 446–455.

Van Rietbergen, B., Weinans, H., Huiskes, R., Odgaard, A., 1995. A new method to determine trabecular bone elastic properties and loading using micromechanical finite-element models. J. Biomech. 28, 69–81.

Verhulp, E., van Rietbergen, B., Huiskes, R., 2006. Comparison of micro-level and continuum-level voxel models of the proximal femur. J. Biomech. 39, 2951–2957.

Zauel, R., Yeni, Y.N., Bay, B.K., Dong, X.N., Fyhrie, D.P., 2006. Comparison of the linear finite element prediction of deformation and strain of human cancellous bone to 3D digital volume correlation measurements. J. Biomech. Eng. 128, 1–6.

Zysset, P., Pahr, D., Engelke, K., Genant, H.K., McClung, M.R., Kendler, D.L., Recknor, C., Kinzl, M., Schwiedrzik, J., Museyko, O., Wang, A., Libanati, C., 2015. Comparison of proximal femur and vertebral body strength improvements in the FREEDOM trial using an alternative finite element methodology. Bone 81, 122–130.

Yang, P.F., Bruggemann, G.P., Rittweger, J., 2011. What do we currently know from in vivo bone strain measurements in humans? J. Musculoskelet. Neuronal Interact. 11, 8–20.